A Variable Structure ADRC for Enhanced Disturbance Rejection and Improved Noise Suppression of PMSM Speed System

Haiyang Cao, *Graduate Student Member, IEEE*, Yongting Deng, *Senior Member, IEEE*,
Yuefei Zuo, *Member, IEEE*, Xiufeng Liu, Jianli Wang, *Member, IEEE*,
and Christopher H. T. Lee, *Senior Member, IEEE*

***Abstract*—It is well-known that there is a trade-off between robustness to disturbances and measurement noise sensitivity in the active disturbance rejection control (ADRC) framework based on extended state observer (ESO). To this end, this article proposes a novel variable structure ADRC (VSADRC) for permanent magnet synchronous motor (PMSM) speed control to enhance the disturbance rejection and the noise suppression simultaneously. In this technology, a variable structure ESO (VSESO) with two-stage interconnected observer is proposed to avoid directly employing noise-contaminated signal, in which the extended disturbance differential is appended to achieve higher-level disturbance estimation. By doing this, at low frequencies, the magnitude curve slope is 40 dB/dec for the VSESO and 20 dB/dec for ESO, while at high frequencies, it is −40 dB/dec for the VSESO and −20 dB/dec for ESO. Furthermore, the stability and output characteristics of the proposed strategy are comprehensively investigated. It is revealed that the superiority of the studied scheme in disturbance rejection and noise suppression. Finally, the experimental results verify the feasibility and effectiveness of the proposed VSADRC.**

***Index Terms*—Active disturbance rejection control (ADRC), disturbance rejection, measurement noise suppression, permanent magnet synchronous motor (PMSM).**

I. INTRODUCTION

WITH the developing requirement for decarbonization, permanent magnet synchronous motor (PMSM) is extensively employed in industrial fields including wind energy systems, ship propulsion and electric vehicles [1], [2], [3]. However, PMSM is subjected to uncertainties, nonlinearities and disturbances, which significantly reduces the control performance of the servo system [4]. Meanwhile, the conventional proportional-integral strategy is difficult to achieve high-performance speed control in presence of exogenous disturbances and endogenous uncertainties. As a result, numerous advanced control techniques, such as predictive control [5], observer-based control [6], and sliding mode control [7] have been carried out for PMSM speed regulation. Among them, the active disturbance rejection control (ADRC) approach has emerged as its robustness against disturbances and it requires minimum model information.

The original ADRC was first proposed by Han in the 1990s [8], which is difficult to implement in engineering practice due to challenges in parameter tuning. To address this, the linear ADRC and bandwidth parameterization strategy are introduced by Gao [9]. Extended state observer (ESO) is the essential component of ADRC strategy which can achieve system state reconstruction and estimation of total disturbance. In order to obtain satisfactory and accurate estimation performance, the ESO usually requires a high-gain form. However, the high gain causes the ESO to be sensitive to measurement noise with high-frequency component [10]. As a result, the noise in the ESO output signal is amplified and is introduced into the closed-loop system based on ADRC control. This may cause vibration or even instability of the PMSM system, which should be avoided [11]. Therefore, there is a trade-off between disturbance rejection and measurement noise suppression in the ESO-based ADRC framework.

Received 9 December 2023; revised 24 March 2024, 30 May 2024, and 6 August 2024; accepted 15 September 2024. Date of publication 22 October 2024; date of current version 3 April 2025. This work was supported in part by the National Nature Science Foundation of China under Grant 12122304, Grant 12473083, and Grant 12303085, in part by Jilin Province Key R&D Plan Project under Grant 20220203036SF, in part by Jilin Province Science and Technology Innovation Platform Project under Grant 20230505007ZP, in part by Jilin Province Science and Technology Development Project under Grant 20240302044GX and Grant 20230203113SF, and in part by the Youth Innovation Promotion Association CAS under Grant Y2023060. *(Corresponding author: Yongting Deng.)*

Haiyang Cao, Xiufeng Liu, and Jianli Wang are with Changchun Institute of Optics, Fine Mechanics, and Physics, Chinese Academy of Sciences, Changchun 130033, China, and also with the University of Chinese Academy of Sciences, Beijing 100049, China (e-mail: caohaiyang20@mails.ucas.ac.cn; liuxiufeng20@mails.ucas.ac.cn; wangjianli@ciomp.ac.cn).

Yongting Deng is with Changchun Institute of Optics, Fine Mechanics, and Physics, Chinese Academy of Sciences, Changchun 130033, China (e-mail: dengyongting@ciomp.ac.cn).

Yuefei Zuo is with the College of Automation Engineering, Nanjing University of Aeronautics and Astronautics, Nanjing 210016, China (e-mail: yuefei.zuo@ieee.org).

Christopher H. T. Lee is with the School of Electrical and Electronic Engineering, Nanyang Technological University, Singapore 639798 (e-mail: chtlee@ntu.edu.sg).

Digital Object Identifier 10.1109/TIE.2024.3468613

Accordingly, numerous investigations in the literature have been developed to address this issue. Typically, the solutions proposed to suppress measurement noise in ADRC can be categorized into three types. The first is the variable gain techniques, which encompass employing adaptive mechanisms [12], adopting nonlinear methods [8], [13], and utilizing intelligent algorithms based on ant colony optimization [14] or deep learning [15]. The essence of this solution is to adopt a high observer gain during transient response to achieve satisfactory disturbance estimation and a low observer gain during steady-state response to mitigate the impact of measurement noise [16]. However, the introduction of adaptive and nonlinear functions complicates theoretical analysis and implementation, and the intelligent algorithms represented by deep learning increase the computational burden. Furthermore, the second option is to introduce additional filters, including integrating filters [17], low-pass filters [18], and Kalman filters [19], which alleviate the adverse effect of measurement noise overamplification while improving disturbance estimation. However, the integrators and low-pass filters cause phase delays to varying degrees, and the composite design of the Kalman filters and ESO increases the complexity of the system.

In addition, a third interesting alternative is to modify the structural design of the observer. For example, a cascaded ESO is proposed to suppress measurement noise by dividing the total disturbance into multiple parts for estimation [20], [21]. Regrettably, the selection guideline of cascade levels is still an unresolved issue [22]. The hybrid cascade-parallel ESO proposed in [23] enhances the perturbation rejection capability, but it requires adaptive gain to cope with measurement noise. In [24], a variable form ESO is presented to improve the robustness of the system. Similarly, a sequential output stacking ESO-based ADRC scheme is devised to achieve steady-state error-free estimation and rejection for disturbances of different orders in [25]. Unfortunately, the aforementioned two methods lack theoretical analysis and verification of measurement noise immunity, which makes industrial practice challenging.

It can be noted that the majority of the existing literature focuses on either disturbance rejection or noise suppression, while relatively few works addressing their simultaneous attenuation. Thankfully, separating the responses of the reference, disturbance, and noise is a promising approach [26], [27], which contributes to quantifying the response characteristics of each input and further investigating directions for optimization [28]. Therefore, this article proposes a variable structure ADRC (VSADRC) based on variable structure ESO (VSESO) to enhance disturbance rejection and improve noise suppression simultaneously for PMSM speed system. The main contributions of this article can be listed as follows.

1) The explicit responses in frequency and time domain based on the ADRC framework are provided to present the trade-off and limitation of conventional ADRC.
2) A novel two-stage interconnected ESO is developed, and then it is combined with the feedback control law to form the proposed VSADRC to simultaneously enhance disturbance rejection and noise immunity.
3) Sufficient analysis based on response separation indicates that the VSADRC offers improved noise suppression, dynamic, steady-state and robust performance.

The rest of this article is organized as follows. Section II presents the PMSM mathematical model and the corresponding conventional ADRC design. Section III exposes the limitation of ADRC and proposes an improved scheme to deal with the trade-off of conventional ADRC. In Section IV, the performance of the studied VSADRC is comprehensively analyzed. The experimental results are presented in Section V. Finally, the conclusion is drawn in Section VI.

II. PMSM DYNAMIC MODEL AND CONVENTIONAL ADRC STRATEGY

A. Mathematical Dynamic Model of PMSM

It is well known that the mathematical dynamic model of PMSM system can be presented as

$$\dot{\Omega}(t) = \frac{1}{J}T_e(t) - \frac{B}{J}\Omega(t) - \frac{1}{J}T_L(t) \tag{1}$$

where $\Omega(t)$ is the mechanical angular speed, J denotes the moment of inertia, B represents the viscous friction torque coefficient, $T_e(t)$ denotes the electromagnetic torque and $T_L(t)$ represents the load torque.

Taking the electromagnetic torque reference $T_e^*(t)$ as the control output, then (1) can be reconstructed in the canonical paradigm as

$$\dot{\Omega}(t) = b_0 T_e^*(t) + f_d(t) \tag{2}$$

where $b = 1/J$ and $b_0 = 1/J_0$ represent the control gain of the plant and its nominal value, respectively. Besides, the lumped disturbance $f_d(t)$ can be specifically expressed as

$$\begin{aligned} f_d(t) = (b - b_0)T_e^*(t) + b(T_e(t) - T_e^*(t)) - \frac{B}{J}\Omega(t) \\ - \frac{1}{J}T_L(t) + f_0(t) \end{aligned} \tag{3}$$

where $(b - b_0)T_e^*(t)$ denotes the disturbance introduced by plant mismatch, $b\,(T_e(t) - T_e^*(t))$ represents the disturbance caused by the electromagnetic torque tracking error, $B\Omega(t)/J$ and $T_L(t)/J$ are the disturbances introduced by viscous friction torque and load torque disturbance, respectively. Besides, $f_0(t)$ is the unknown endogenous and exogenous disturbance.

B. Conventional ADRC Method Design

In the ADRC architecture, the lumped disturbance is considered as a new extended state. According to the motion equation in (2), the extended state-space model can be constructed as

$$\begin{cases} \begin{bmatrix} \dot{\Omega}(t) \\ \dot{f}_d(t) \end{bmatrix} = \begin{bmatrix} 0 & 1 \\ 0 & 0 \end{bmatrix} \begin{bmatrix} \Omega(t) \\ f_d(t) \end{bmatrix} + \begin{bmatrix} b_0 \\ 0 \end{bmatrix} T_e^*(t) + \begin{bmatrix} 0 \\ 1 \end{bmatrix} \varphi_e(t) \\ \Omega_m(t) = \Omega(t) + \xi(t) \end{cases} \tag{4}$$

where $\varphi_e(t)$ is the first derivative of $f_d(t)$ and $\Omega_m(t)$ denotes the speed measurement output. Besides, $\xi(t)$ represents the measurement noise, which is unavoidable owing to the quantization error in the position measurement.

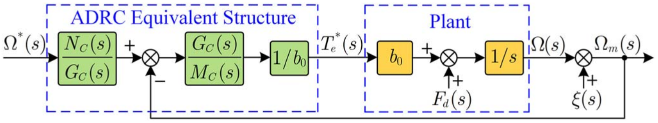

Fig. 1. Equivalent structure diagram of the conventional ADRC.

Then, the conventional ESO can be designed on the basis of (4) as

$$\begin{bmatrix}\dot{z}_1(t)\\ \dot{z}_2(t)\end{bmatrix} = \begin{bmatrix}-\beta_1 & 1\\ -\beta_2 & 0\end{bmatrix}\begin{bmatrix}z_1(t)\\ z_2(t)\end{bmatrix} + \begin{bmatrix}b_0 & \beta_1\\ 0 & \beta_2\end{bmatrix}\begin{bmatrix}T_e^*(t)\\ \Omega_m(t)\end{bmatrix} \tag{5}$$

where $z_1(t)$ and $z_2(t)$ are the estimated value of $\Omega(t)$ and $f_d(t)$, respectively. In addition, β_1 and β_2 are the gains of the ESO, which can be described according to the pole configuration strategy [9] as

$$\beta_i = \frac{2!}{(2-i)!\,i!}\omega_o^i,\ i = 1, 2 \tag{6}$$

where ω_o denotes the bandwidth of the ESO.

Afterwards, the variables estimated by the conventional ESO are employed to construct the linear state error feedback, so the control law can be obtained as

$$T_e^*(t) = \frac{K_P(\Omega^*(t) - z_1(t)) - z_2(t)}{b_0} \tag{7}$$

where $\Omega^*(t)$ is the mechanical angular speed reference and K_P denotes the proportional gain of the controller.

III. Problem Formulation and Scheme Design

A. Limitation Analysis of Conventional ADRC

In this subsection, the performance of disturbance estimation and noise suppression in the conventional ADRC framework is sufficiently analyzed, and the explicit expressions are provided to illustrate the limitations of conventional ADRC.

The estimated values $Z_1(s)$ and $Z_2(s)$ of ESO with respect to the inputs $\Omega^*(s)$ and $T_e^*(s)$ of the observer system based on (5) can be deduced in the frequency domain as

$$\begin{cases} Z_1(s) = \dfrac{\beta_1 s + \beta_2}{s^2 + \beta_1 s + \beta_2}\Omega_m(s) + \dfrac{b_0 s}{s^2 + \beta_1 s + \beta_2}T_e^*(s) \\[2ex] Z_2(s) = \dfrac{\beta_2 s}{s^2 + \beta_1 s + \beta_2}\Omega_m(s) - \dfrac{b_0\beta_2}{s^2 + \beta_1 s + \beta_2}T_e^*(s) \end{cases}. \tag{8}$$

According to the architecture in [27] and [28], the conventional ADRC can be equivalent to a two-degree-of-freedom structure as shown in Fig. 1. Then, combining (7) and (8), the control law can be derived in the frequency domain as

$$T_e^*(s) = \frac{N_C(s)}{b_0 M_C(s)}\Omega^*(s) - \frac{G_C(s)}{b_0 M_C(s)}\Omega_m(s) \tag{9}$$

where

$$N_C(s) = K_P(s^2 + \beta_1 s + \beta_2),\ M_C(s) = s(s + \beta_1 + K_P)$$
$$G_C(s) = (\beta_2 + \beta_1 K_P)s + \beta_2 K_P.$$

Then, substituting (6) into (9), the total output $\Omega_m(s)$ of the system can be obtained as

$$\Omega_m(s) = \Phi_T^C(s)\Omega^*(s) + \Phi_F^C(s)F_d(s) + \Phi_\xi^C(s)\xi(s) \tag{10}$$

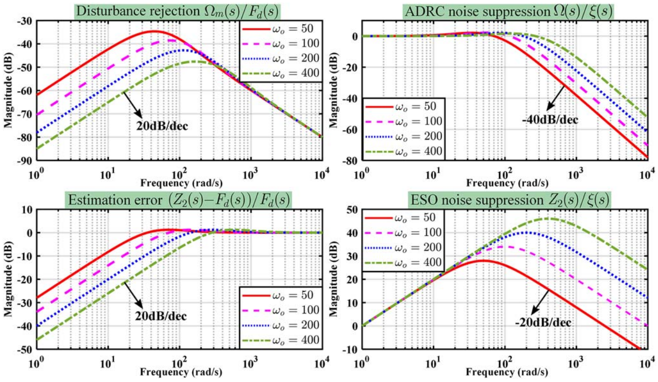

Fig. 2. Frequency domain responses of the conventional ADRC and ESO to disturbance and noise under different ω_o (rad/s).

where

$$\begin{cases} \Phi_T^C(s) = \dfrac{\Omega_m^{ct}(s)}{\Omega^*(s)} = \dfrac{N_C(s)}{sM_C(s) + G_C(s)} = \dfrac{K_P}{s + K_P} \\[2ex] \Phi_F^C(s) = \dfrac{\Omega_m^{cf}(s)}{F_d(s)} = \dfrac{M_C(s)}{sM_C(s) + G_C(s)} = \dfrac{s(s + 2\omega_o + K_P)}{(s + K_P)(s + \omega_o)^2} \\[2ex] \Phi_\xi^C(s) = \dfrac{\Omega_m^{c\xi}(s)}{\xi(s)} = \dfrac{sM_C(s)}{sM_C(s) + G_C(s)} = \dfrac{s^2(s + 2\omega_o + K_P)}{(s + K_P)(s + \omega_o)^2} \end{cases}.$$

It can be seen that the total output includes the three-term response of tracking, disturbance and noise. Obviously, disturbance and noise are unfavorable factors that affect the system output to track the reference accurately, which need to be suppressed and eliminated.

In addition, from (8) for the conventional ESO, the transfer functions from the measurement noise $\xi(s)$ to the estimated disturbance Z_2(s), and from the actual disturbance $F_d(s)$ to the disturbance estimation error $E_2(s)$ can be deduced as

$$\begin{cases} \Phi_\xi^{co}(s) = \dfrac{Z_2(s)}{\xi(s)} = \dfrac{\omega_o^2 s}{(s + \omega_o)^2} \\[2ex] \Phi_F^{co}(s) = \dfrac{E_2(s)}{F_d(s)} = \dfrac{Z_2(s) - F_d(s)}{F_d(s)} = -\dfrac{s(s + 2\omega_o)}{(s + \omega_o)^2} \end{cases}. \tag{11}$$

Selecting the proportional gain $K_P = 100$, the frequency responses of disturbance and noise for the conventional ADRC and ESO with different ω_o are presented in Fig. 2. In practice, disturbance signals are often low-frequency components, while noise signals are usually high-frequency components. It can be seen that with the ESO bandwidth increases, the disturbance rejection capability of ADRC and the disturbance estimation error property of ESO are improved, and the slopes of their magnitude curves are 20 dB/dec at low frequencies. However, the noise suppression ability of the conventional ADRC and ESO decreases with the increase of ESO bandwidth, and the slopes of their magnitude curves are −40 and −20 dB/dec at high frequencies, respectively. Thus, there is a trade-off between the low-frequency disturbance rejection and high-frequency noise suppression.

In order to further illustrate the disturbance rejection performance of the conventional ESO and ADRC, Fig. 3 plots their time-domain responses under different disturbances with $K = 1$

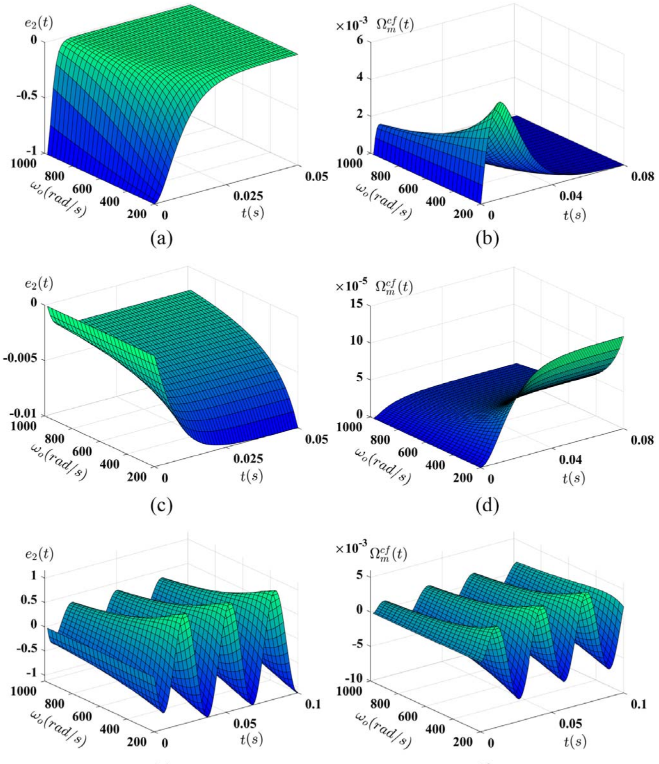

(a) (b)

(c) (d)

(e) (f)

Fig. 3. Time domain responses of the ESO and ADRC to different disturbances with various ω_o. The ESO response is on the left and the ADRC response is on the right. (a) and (b) for $f_d(t) = K$. (c) and (d) for $f_d(t) = Kt$. (e) and (f) for $f_d(t) = K\sin(\omega_h t)$, where $\omega_h = 200$ (rad/s).

according to $\Phi_F^{co}(s)$ and $\Phi_F^{C}(s)$. It can be found that in the time domain, the disturbance estimation error of ESO and the output disturbance of ADRC can converge to zero only under step disturbance $F_d(s) = K/s$, which can also be verified from the final value theorem as $\lim_{t\to\infty} e_2(t) = \lim_{s\to 0} s\Phi_F^{co}(s)F_d(s)$ and $\lim_{t\to\infty}\Omega_m^{cf}(t) = \lim_{s\to 0} s\Phi_F^{C}(s)F_d(s)$. Furthermore, there is an obvious oscillatory response under periodic disturbance from Fig. 3(e) and 3(f). In addition, it can be found that the steady-state offset of nonstep disturbances cannot be completely eliminated by increasing the observer bandwidth greatly, which is also unrealistic. Therefore, it is necessary to investigate a novel ADRC structure to alleviate the steady-state deviation of nonstep disturbances and suppress the measurement noise.

B. Design of the Proposed VSADRC Scheme

In order to enhance the rejection capability to the various disturbances and improve the suppression performance of measurement noise, a novel VSADRC scheme for PMSM speed loop is proposed in this subsection.

First, for the accurate real-time estimation of total disturbance and effective noise suppression, a VSESO with two-stage interconnected subsystems is proposed, which is closely related to the performance of the VSADRC. The corresponding first-stage subsystem VSESO1 is constructed as

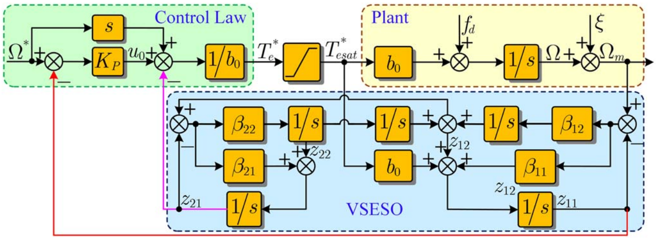

Fig. 4. Schematic diagram of the VSADRC based on VSESO.

$$\begin{bmatrix}\dot z_{11}(t)\\ \dot z_{12}(t)\end{bmatrix} = \begin{bmatrix}-\beta_{11} & 1\\ -\beta_{12} & 0\end{bmatrix}\begin{bmatrix}z_{11}(t)\\ z_{12}(t)\end{bmatrix} + \begin{bmatrix}b_0 & \beta_{11} & 0\\ 0 & \beta_{12} & 1\end{bmatrix}\begin{bmatrix}T_e^*(t)\\ \Omega_m(t)\\ z_{22}(t)\end{bmatrix}. \tag{12}$$

It can be noted that the $z_{22}(t)$ signal from VSESO2 is employed in the construction of VSESO1. Meanwhile, $z_{12}(t)$ from VSESO1 is the only input signal to design the second-stage subsystem VSESO2 that is established as

$$\begin{bmatrix}\dot z_{21}(t)\\ \dot z_{22}(t)\end{bmatrix} = \begin{bmatrix}-\beta_{21} & 1\\ -\beta_{22} & 0\end{bmatrix}\begin{bmatrix}z_{21}(t)\\ z_{22}(t)\end{bmatrix} + \begin{bmatrix}\beta_{21}\\ \beta_{22}\end{bmatrix} z_{12}(t) \tag{13}$$

where $z_{12}(t)$ is the pre-estimation of $f_d(t)$, and $z_{11}(t)$, $z_{21}(t)$ and $z_{22}(t)$ are the final estimated values of $\Omega(t)$, $f_d(t)$, and $\varphi_e(t)$, respectively. Besides, β_{11}, β_{12}, β_{21}, and β_{22} denote the observer gains, and their reasonable choice can effectively reconstruct various states of the plant.

Similarly, the pole configuration strategy is also adopted to tune the gain coefficients of the VSESO, which satisfies

$$\beta_{1i} = \beta_{2i} = \frac{2!}{(2-i)!\, i!}\omega_o^i,\ i = 1, 2. \tag{14}$$

Afterwards, the control law of VSADRC is constructed according to the feedback control. The speed tracking error can be presented as $e_s(t) = \Omega^*(t) - \Omega(t)$, then

$$\dot e_s(t) = \dot\Omega^*(t) - \dot\Omega(t) = \dot\Omega^*(t) - b_0 T_e^*(t) - f_d(t). \tag{15}$$

From the feedback control, the desired error convergence law can be written as

$$\dot e_s(t) = -K_P e_s(t). \tag{16}$$

Then, substituting (16) into (15), and $\Omega(t)$ and $f_d(t)$ are replaced by their estimated values $z_{11}(t)$ and $z_{21}(t)$, then the control law with reference differential feedforward can be implemented as

$$T_e^*(t) = b_0^{-1}\left[\dot\Omega^*(t) + K_P(\Omega^*(t) - z_{11}(t)) - z_{21}(t)\right]. \tag{17}$$

Accordingly, with the required states accurately estimated in real-time, the schematic diagram of the VSADRC based on the VSESO is depicted in Fig. 4.

IV. PERFORMANCE ANALYSIS

A. Convergence Analysis of VSESO

According to (4) and (12), the observation error of VSESO1 can be obtained as

$$\begin{cases} \dot{e}_{11}(t) = \dot{z}_{11}(t) - \dot{\Omega}(t) = e_{12}(t) - \beta_{11}e_{11}(t) + \beta_{11}\xi(t) \\ \dot{e}_{12}(t) = \dot{z}_{12}(t) - \dot{f}_d(t) = z_{22}(t) - \beta_{12}e_{11}(t) - \varphi_e(t) + \beta_{12}\xi(t). \end{cases} \tag{18}$$

Let $\eta_i(t) = e_{1i}/\omega_o^{i-1}$, $i = 1, 2$, then (18) results in

$$\dot{\boldsymbol{\eta}}(t) = \omega_o \boldsymbol{A}\boldsymbol{\eta}(t) + (\varphi_e(t) - z_{22}(t))\boldsymbol{K}/\omega_o + \omega_o \boldsymbol{H}\xi(t) \tag{19}$$

where

$$\boldsymbol{\eta}(t) = \begin{bmatrix} \eta_1(t) \\ \eta_2(t) \end{bmatrix}, \boldsymbol{A} = \begin{bmatrix} -2 & 1 \\ -1 & 0 \end{bmatrix}, \boldsymbol{K} = \begin{bmatrix} 0 \\ -1 \end{bmatrix}, \boldsymbol{H} = \begin{bmatrix} 2 \\ 1 \end{bmatrix}.$$

Since both the eigenvalues of $\boldsymbol{A}$ are -1, $\boldsymbol{A}$ demonstrates Hurwitz stable. Subsequently, a symmetric positive definite matrix $\boldsymbol{P}$ exists and satisfies that

$$\boldsymbol{A}^{\boldsymbol{T}}\boldsymbol{P} + \boldsymbol{P}\boldsymbol{A} = -\boldsymbol{I} \tag{20}$$

where $\boldsymbol{P} = \begin{bmatrix} (1/2) & -(1/2) \\ -(1/2) & (3/2) \end{bmatrix}$. Select $\boldsymbol{V}(\boldsymbol{\eta}(t)) = \boldsymbol{\eta}^T(t)\boldsymbol{P}\boldsymbol{\eta}(t)$ as a Lyapunov function and taking derivative along (17), we obtain

$$\begin{aligned} \dot{\boldsymbol{V}}(\boldsymbol{\eta}(t)) &= \dot{\boldsymbol{\eta}}^T(t)\boldsymbol{P}\boldsymbol{\eta}(t) + \boldsymbol{\eta}^T(t)\boldsymbol{P}\dot{\boldsymbol{\eta}}(t) \\ &= -\omega_o\|\boldsymbol{\eta}(t)\|^2 + 2\omega_o^{-1}\boldsymbol{\eta}^T(t)\boldsymbol{P}\boldsymbol{K}(\varphi_e(t) - z_{22}(t)) \\ &\quad + 2\omega_o\boldsymbol{\eta}^T(t)\boldsymbol{P}\boldsymbol{H}\xi(t). \end{aligned} \tag{21}$$

Define $\boldsymbol{x}(t) = [\Omega(t), f_d(t)]^T$ and assume the measurement noise $\xi(t)$ is bounded, since $\varphi_e(t)$ and $\xi(t)$ are globally Lipschitz in terms of $\boldsymbol{x}(t)$, that is, there exists two constants σ_1 and σ_2 such that $|\varphi_e(t) - z_{22}(t)| \le \sigma_1 \|\boldsymbol{x}(t) - \boldsymbol{z}_{\boldsymbol{1i}}(t)\|$ and $\xi(t) \le \sigma_2 \|\boldsymbol{x}(t) - \boldsymbol{z}_{\boldsymbol{1i}}(t)\|$ for all $\boldsymbol{x}(t), \boldsymbol{z}_{\boldsymbol{1i}}(t)$, then

$$\begin{aligned} &2\omega_o^{-1}\boldsymbol{\eta}^T(t)\boldsymbol{P}\boldsymbol{K}\,|\varphi_e(t) - z_{22}(t)| \\ &\quad \le 2\sigma_1\omega_o^{-1}\boldsymbol{\eta}^T(t)\boldsymbol{P}\boldsymbol{K}\,\|\boldsymbol{x}(t) - \boldsymbol{z}_{\boldsymbol{1i}}(t)\| \end{aligned} \tag{22}$$

$$2\omega_o\boldsymbol{\eta}^T(t)\boldsymbol{P}\boldsymbol{H}\xi(t) \le 2\sigma_2\omega_o\boldsymbol{\eta}^T(t)\boldsymbol{P}\boldsymbol{H}\,\|\boldsymbol{x}(t) - \boldsymbol{z}_{\boldsymbol{1i}}(t)\|. \tag{23}$$

When $\omega_o \ge 1$, we have $\omega_o^{-1}\|\boldsymbol{x}(t) - \boldsymbol{z}_{\boldsymbol{1i}}(t)\| = \omega_o^{-1}\|\boldsymbol{e}_{\boldsymbol{1i}}(t)\| \le \|\boldsymbol{\eta}(t)\|$. Meanwhile, $\|\boldsymbol{P}\boldsymbol{K}\sigma_1\|^2 - 2\|\boldsymbol{P}\boldsymbol{K}\sigma_1\| + 1 \ge 0$ and $\|\boldsymbol{P}\boldsymbol{H}\sigma_2\omega_o\|^2 - 2\|\boldsymbol{P}\boldsymbol{H}\sigma_2\omega_o\| + 1 \ge 0$. Thus, one has

$$\begin{cases} 2\omega_o^{-1}\boldsymbol{\eta}^T(t)\boldsymbol{P}\boldsymbol{K}\,|\varphi_e(t) - z_{22}(t)| \le \delta_1\|\boldsymbol{\eta}(t)\|^2 \\ 2\omega_o\boldsymbol{\eta}^T(t)\boldsymbol{P}\boldsymbol{H}\xi(t) \le \delta_2\|\boldsymbol{\eta}(t)\|^2 \end{cases} \tag{24}$$

with $\delta_1 = \|\boldsymbol{P}\boldsymbol{K}\sigma_1\|^2 + 1$ and $\delta_2 = \|\boldsymbol{P}\boldsymbol{H}\sigma_2\omega_o\|^2 + 1$. Substituting (24) into (21), we have

$$\dot{\boldsymbol{V}}(\boldsymbol{\eta}(t)) \le -(\omega_o - (\delta_1 + \delta_2))\|\boldsymbol{\eta}(t)\|^2 \tag{25}$$

that is, $\dot{\boldsymbol{V}}(\boldsymbol{\eta}(t)) < 0$ if $\omega_o > (\delta_1 + \delta_2)$ and ω_o is positive. Accordingly, it is obvious that ω_o meets the high gain requirement. Analogously, let $e_{2i}(t) = z_{2i}(t) - x_i(t)$ as the observation error of the VSESO2, the same deduction as (25) can be computed. Thus, we obtain

$$\lim_{t\to\infty} e_{1i}(t) = 0, \lim_{t\to\infty} e_{2i}(t) = 0, i = 1, 2. \tag{26}$$

Accordingly, it can be noted that asymptotic analysis in the sense of Lyapunov holds. Hence, the equilibrium of the proposed VSESO is asymptotically stable.

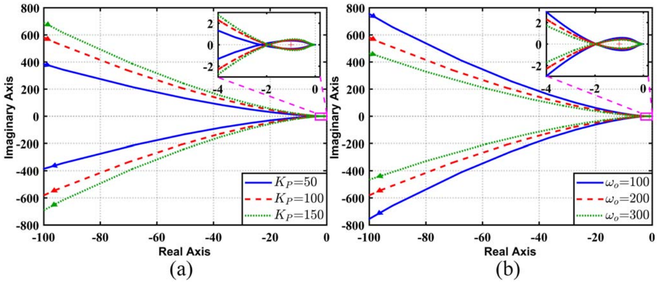

Fig. 5. Nyquist curves of the system with the studied VSADRC scheme. (a) $\omega_o = 200$; (b) $K_P = 100$.

B. Closed-Loop System Stability Analysis

Similar to (9), the VSADRC can also be equivalent to a two-degree-of-freedom structure. Combining (12), (13), and (17), the control law can be derived in the frequency domain as

$$T_e^*(s) = \frac{N_V(s)}{b_0 M_V(s)}\Omega^*(s) - \frac{G_V(s)}{b_0 M_V(s)}\Omega_m(s) \tag{27}$$

where

$$\begin{aligned} N_V(s) &= ((s+\omega_o)^4 - \omega_o^2(s^2 + 2\omega_o s))(s+\omega_o)^2(K_P + s) \\ M_V(s) &= s^2(s+\omega_o)^2(s^2 + 4\omega_o s + K_P s + 5\omega_o^2 + 2K_P\omega_o) \\ G_V(s) &= \omega_o(s+\omega_o)^2(K_P(2s^3 + 5\omega_o s^2 + 2\omega_o^2 s + \omega_o^3) \\ &\quad + 2\omega_o^2 s^2 + \omega_o^3 s). \end{aligned}$$

According to the analogy of Fig. 1, the open-loop transfer function of the VSADRC-based system can be expressed as

$$\begin{aligned} G_o(s) &= \frac{G_V(s)}{M_V(s)}\frac{1}{s} \\ &= \frac{\omega_o(K_P(2s^3 + 5\omega_o s^2 + 2\omega_o^2 s + \omega_o^3) + 2\omega_o^2 s^2 + \omega_o^3 s)}{s^3(s^2 + 4\omega_o s + K_P s + 5\omega_o^2 + 2K_P\omega_o)}. \end{aligned} \tag{28}$$

It can be seen from (28) that the stability of the system is closely related to two parameters, i.e., K_P and ω_o. Fig. 5 presents the Nyquist curves of the system based on the studied VSADRC scheme under the two parameters change. From Fig. 5, the closed-loop system employing the VSADRC is stable, evidenced by the absence of open-loop poles in the right half of the s-plane and an equal number of encirclements around the critical point (−1,0), both clockwise and counterclockwise. Furthermore, the impact of parameters variation on the system stability of the proposed scheme is limited. Thus, the whole closed-loop system based on VSADRC is stable.

C. Disturbance and Noise Analysis in Frequency Domain

As the core component of VSADRC, the proposed VSESO introduces an extended estimation of the disturbance derivative to promote the disturbance attenuation of the output response. In addition, VSESO adopts a two-stage interconnection structure, in which the subsequent stage utilizes the estimation of the previous stage as reference signal to avoid using the signal directly polluted by noise, which means that the final estimation has better noise immunity. The analysis details of disturbance rejection and noise suppression of VSADRC from frequency domain are as follows.

Similar to (11), according to (12) and (13), the transfer functions of the VSESO from the measurement noise $\xi(s)$ to the estimated disturbance $Z_{21}(s)$, and from the actual disturbance $F_d(s)$ to the disturbance estimation error $E_{12}(s)$ can be derived as

$$\begin{cases} \Phi_{\xi}^{vo}(s) = \dfrac{Z_{21}(s)}{\xi(s)} = \dfrac{s(2\omega_o^3 s + \omega_o^4)}{(s+\omega_o)^4 - \omega_o^2 s^2 - 2\omega_o^3 s} \\ \Phi_{F}^{vo}(s) = \dfrac{E_{12}(s)}{F_d(s)} = -\dfrac{s^2(s^2 + 4\omega_o s + 5\omega_o^2)}{(s+\omega_o)^4 - \omega_o^2 s^2 - 2\omega_o^3 s} \end{cases}. \quad (29)$$

Then, the total output $\Omega_m(s)$ of the system is similar to the derivation of (10) and can be expressed as

$$\Omega_m(s) = \Phi_T^V(s)\Omega^*(s) + \Phi_F^V(s)F_d(s) + \Phi_\xi^V(s)\xi(s) \quad (30)$$

where

$$\begin{cases} \Phi_T^V(s) = \dfrac{\Omega_m^{vt}(s)}{\Omega^*(s)} = \dfrac{N_V(s)}{sM_V(s) + G_V(s)} = 1 \\ \Phi_F^V(s) = \dfrac{\Omega_m^{vf}(s)}{F_d(s)} = \dfrac{s^2(s^2 + 4\omega_o s + K_P s + 2\omega_o^2 + 2K_P\omega_o)}{((s+\omega_o)^4 - \omega_o^2(s^2 + 2\omega_o s))(K_P + s)} \\ \Phi_\xi^V(s) = \dfrac{\Omega_m^{v\xi}(s)}{\xi(s)} = \dfrac{s^3(s^2 + 4\omega_o s + K_P s + 2\omega_o^2 + 2K_P\omega_o)}{((s+\omega_o)^4 - \omega_o^2(s^2 + 2\omega_o s))(K_P + s)} \end{cases}.$$

Selecting the same parameters as in Fig. 2, the frequency responses of disturbance and noise for the proposed VSADRC and VSESO with different ω_o are shown in Fig. 6. It can be noted that the slopes of the magnitude curves of the VSADRC disturbance rejection and the VSESO disturbance estimation error are both 40 dB/dec, and the corresponding slopes of noise suppression magnitude curves are both −40 dB/dec. Compared with Fig. 2, when the same ω_o is employed, the disturbance rejection performance of VSADRC and VSESO at low frequencies and the noise suppression property at high frequencies are better than those of the conventional ADRC and ESO. For example, when ω_o is set to 200 rad/s for both VSESO and ESO, the magnitude of estimation error approximates −40 dB for the ESO and −80 dB for the VSESO at low frequency 1 rad/s, and the magnitude of noise suppression approximates 12 dB for the ESO and −18 dB for the VSESO at high frequency 10^4 rad/s. Therefore, the proposed VSESO-based VSADRC scheme is able to achieve stronger disturbance suppression and noise attenuation simultaneously.

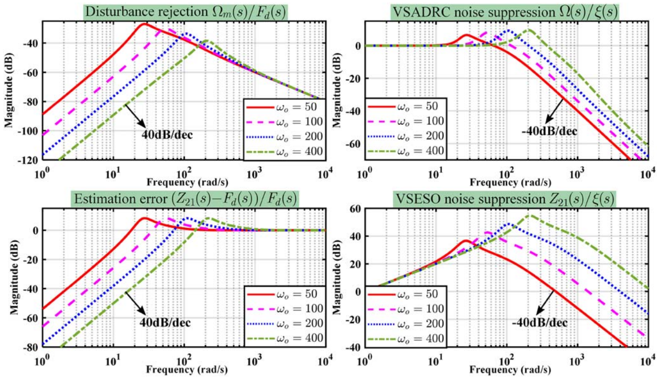

Fig. 6. Frequency domain responses of the proposed VSADRC and VSESO to disturbance and noise under different ω_o (rad/s).

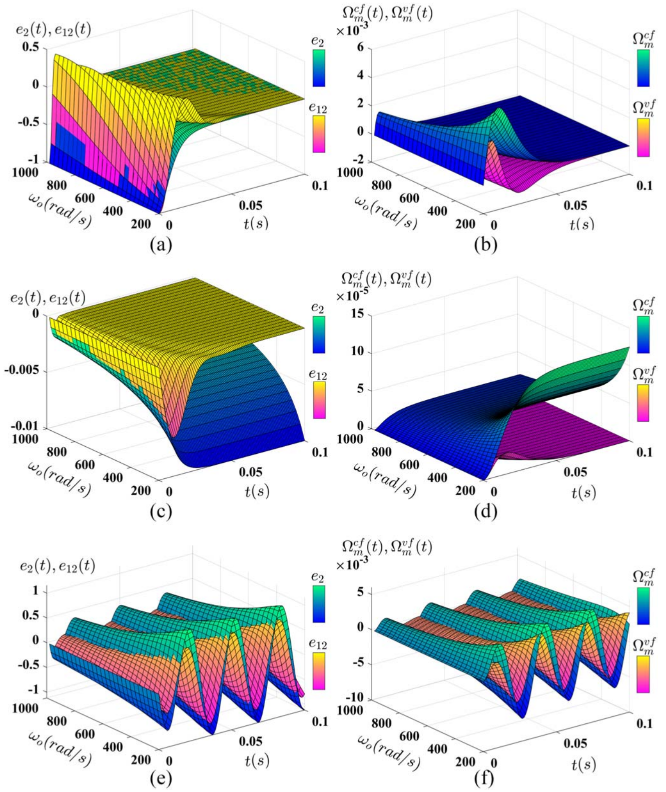

Fig. 7. Time domain responses comparison for two types of observers and controllers to different disturbances with various ω_o. The comparison of ESO and VSESO is on the left, and the comparison of ADRC and VSADRC is on the right. (a) and (b) for $f_d(t) = K$. (c) and (d) for $f_d(t) = Kt$. (e) and (f) for $f_d(t) = K\sin(\omega_h t)$, where $\omega_h = 200$(rad/s).

D. Disturbance Responses Analysis from Time Domain

The dynamic outputs $e_2(t)$ and $e_{12}(t)$ of ESO and VSESO can be obtained from (11) and (29) respectively, and the dynamic outputs $\Omega_m^{cf}(t)$ and $\Omega_m^{vf}(t)$ of ADRC and VSADRC can be obtained from (10) and (30) respectively, as presented in Fig. 7. Meanwhile, the final value expressions of VSESO on disturbance estimation error and VSADRC on disturbance suppression can be established as

$$\begin{cases} e_{12}(\infty) = \lim\limits_{s\to 0} -\dfrac{s^3(s^2+4\omega_o s^3+5\omega_o^2 s^2)}{(s+\omega_o)^4-\omega_o^2 s^2-2\omega_o^3 s}F_d(s) \\ \Omega_m^{vf}(\infty) = \lim\limits_{s\to 0} \dfrac{s^3(s^2+4\omega_o s+K_P s+2\omega_o^2+2K_P\omega_o)}{((s+\omega_o)^4-\omega_o^2(s^2+2\omega_o s))(K_P+s)}F_d(s) \end{cases}. \tag{31}$$

From Fig. 7, for step disturbance $F_d(s) = K/s$, both types of observer and both types of controller have no steady-state error. With regard to ramp disturbance $F_d(s) = K/s^2$, there are steady-state errors in the output dynamic of the conventional ESO and ADRC, while the responses of the proposed VSESO and VSADRC can converge to zero, which is also confirmed by (31). This is because the proposed scheme introduces one more zero point in the disturbance estimation error and disturbance suppression transfer function compared with the conventional ADRC method. In addition, it can be seen from Fig. 7(e) and (f) that although the proposed method cannot completely eliminate the oscillatory response, the magnitudes of the oscillatory response are significantly reduced compared with the conventional ADRC strategy. By that analogy, the responses of the proposed VSESO and VSADRC cannot completely converge to zero when dealing with more complex disturbance, but they can significantly improve the suppression effect compared with the conventional ESO and ADRC method.

Evidently, the proposed VSESO-based VSADRC eliminates the response error of ramp disturbance by introducing the extended estimation of the disturbance derivative, so that the proposed scheme can achieve a higher level of disturbance estimation and suppression accuracy, and thereby achieving the purpose of enhancing disturbance rejection.

E. Dynamic Performance Under Parameter Mismatch

The control gain is a significant parameter under the ADRC framework, and its changes affect PMSM system performance. Thus, it is necessary to investigate the impact of control gain mismatch on the performance of the proposed scheme.

According to (2), the plant with the control gain mismatch can be expressed as

$$s\Omega(s) = F_d^{'}(s) + bT_e^*(s) \tag{32}$$

where $F_d^{'}(s)$ represents the total disturbance excluding model mismatch. Then, the transfer function from input to output of the proposed VSADRC can be presented as

$$\Phi_T^V(s) = \frac{\Omega_m(s)}{\Omega^*(s)} = \frac{N_V(s)}{sM_V(s)r_b + G_V(s)} \tag{33}$$

where $r_b = b_0/b$. Similarly, the transfer function from input to output of the conventional ADRC can be derived as

$$\Phi_T^C(s) = \frac{K_P(s+\omega_o)^2}{s^2(s+2\omega_o+K_P)r_b + (\omega_o^2+2\omega_o K_P)s + \omega_o^2 K_P}. \tag{34}$$

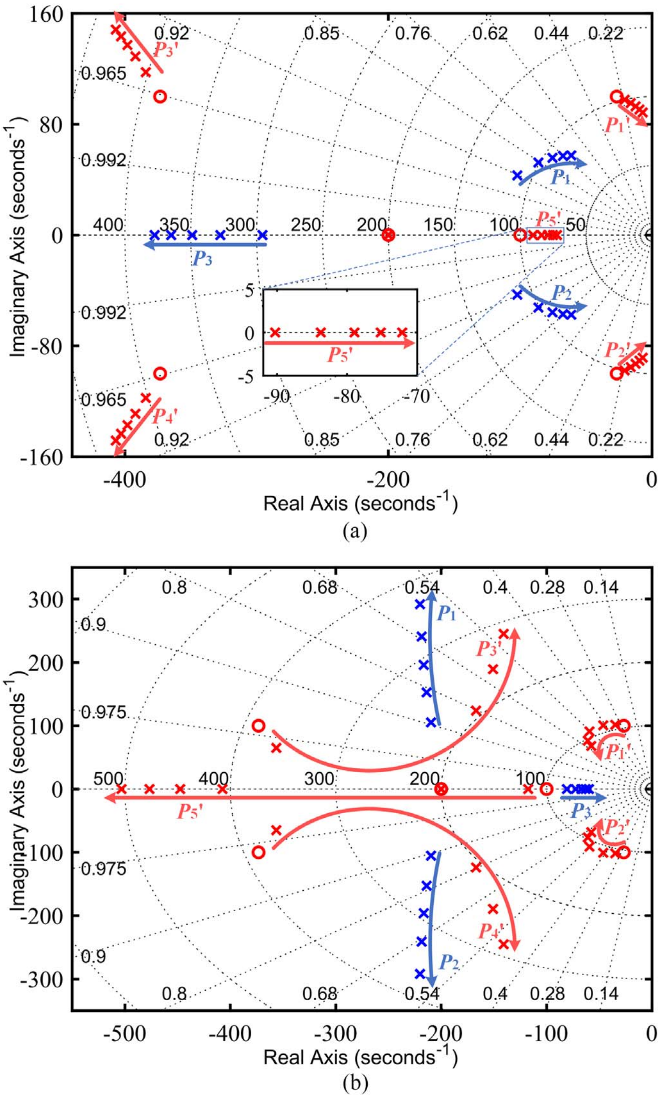

Fig. 8. The pole-zero distribution diagram using ADRC (blue color) and VSADRC (red color). (a) Incremental r_b under $r_b > 1$. (b) Decremental r_b under $0 < r_b < 1$.

Fig. 8 shows the poles and zeros distribution diagram of the closed-loop system using the conventional ADRC and the proposed VSADRC method, where the crosses denote poles and the cycles denote zeros. There are three blue poles (P_1, P_2, and P_3) from (34) and five red poles ($P_1^{'}$, $P_2^{'}$, $P_3^{'}$, $P_4^{'}$, and $P_5^{'}$) from (33), which determine the performance of the corresponding controller. It can be seen from Fig. 8(a) that when $r_b > 1$, with r_b increasing, the two dominant poles (P_1 and P_2) of ADRC and the three dominant poles ($P_1^{'}$, $P_2^{'}$, and $P_5^{'}$) of VSADRC gradually approach the imaginary axis, which means that the recovery time of both controllers increases. When $b_0 < b$, as shown in Fig. 8(b), with r_b decreasing, the pole P_3 of ADRC moves to the right, which causes the recovery time to increase, and the damping of P_1 and P_2 decreases, which introduces the response oscillation. In contrast, the dominant poles $P_1^{'}$ and $P_2^{'}$ of VSADRC are shifted to the left, which reduces the recovery time. Furthermore, the dominant poles of VSADRC move closer to the real axis, which increases damping to reduce the oscillation.

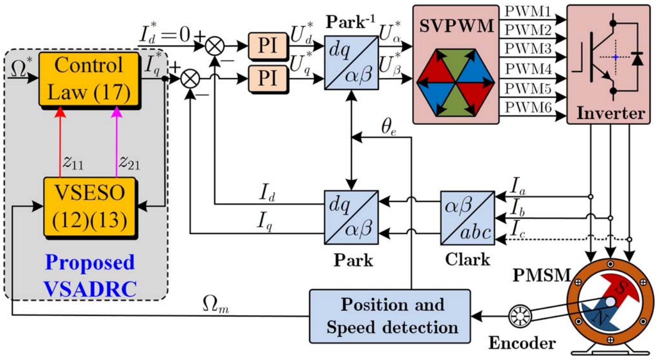

Fig. 9. Structural diagram of PMSM drives with the proposed VSADRC.

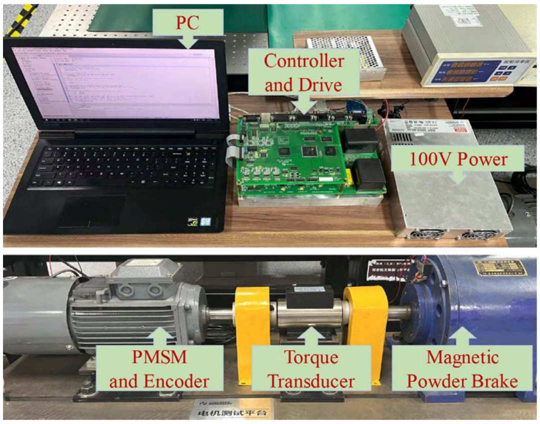

Fig. 10. PMSM experimental setup.

TABLE I
KEY SPECIFICATIONS OF THE EXPERIMENTAL PMSM

Symbols	Parameters	Values	Units
ψ_f	Rotor flux linkage	0.29	Wb
L_s	dq-axis inductance	6.5	mH
R_s	Stator resistance	0.675	Ohm
J	Inertia	0.0425	Kg·m^2
p_n	Pole pairs	3	–
Ω_N	Rated speed	1200	rpm
T_L	Rated torque	6	N·m
U_N	DC-bus voltage	100	V
I_N	Rated current	5	A

In addition, it can be seen that there is a zero point around each of the four poles $P_1' - P_4'$ of the proposed method, which can cancel or weaken the effect of these four poles to enhance the robustness of the system. However, the distance between the two poles P_1 and P_2 of the conventional ADRC and the zero point is relatively large, and the variations in pole locations have a greater impact on the closed-system, which makes it less robust than the proposed VSADRC scheme.

V. EXPERIMENTAL VERIFICATION

To investigate the feasibility and superiority of the proposed VSADRC, the fairness comparison between conventional ADRC and PI controller is first discussed, and then a series of experimental verifications are performed. Fig. 9 presents the whole structure diagram of the proposed VSADRC under the field-oriented control framework. The studied algorithm is used in the speed outer loop, and the conventional PI controller is employed in the current inner loop of PMSM.

A. Comparative Study on Fairness of ADRC and PI

There is no unified standard for fairness experimental comparison between conventional ADRC and PI, which has troubled many scholars. In order to compare the fairness of the experiment in the next subsection, this subsection presents a rigorous justification comparison method through the two-degree-of-freedom structure of ADRC, so that the parameter settings of ADRC and PI are uniquely corresponding.

According to the two-degree-of-freedom structure of ADRC in Fig. 1, let $H(s) = (N_C(s)/G_C(s))$, $C(s) = (G_C(s)/b_0 M_C(s))$, then $H(s)$ and $C(s)$ can be expressed as

$$\begin{cases} H(s) = \dfrac{N_C(s)}{G_C(s)} = \dfrac{K_P(s^2 + \beta_1 s + \beta_2)}{(\beta_2 + \beta_1 K_P)s + \beta_2 K_P} \\ C(s) = \dfrac{G_C(s)}{b_0 M_C(s)} = \dfrac{(\beta_2 + \beta_1 K_P)s + \beta_2 K_P}{b_0 s(s + \beta_1 + K_P)} \end{cases}. \tag{35}$$

Then, $C(s)$ can be rewritten as

$$C(s) = C_{PI}(s) F_L(s) \tag{36}$$

where

$$C_{PI}(s) = k_{ps} + k_{is}\frac{1}{s}, F_L(s) = \frac{\beta_1 + K_P}{s + \beta_1 + K_P}$$

$$k_{ps} = \frac{\beta_2 + \beta_1 K_P}{b_0(\beta_1 + K_P)}, k_{is} = \frac{\beta_2 K_P}{b_0(\beta_1 + K_P)}.$$

In Fig. 1, the prefilter $H(s)$ has no impact on the feedback characteristics [29]. Thus, the conventional ADRC can be equivalent to a PI controller and a first-order low-pass filter, and the similar conclusion can be found in [27], [28], and [30]. In addition, it can be from (36) concluded that each set of ADRC parameters can obtain unique PI parameters, which is the most popular comparison criterion at present. Moreover, it can also be verified from (36) that ADRC has a stronger capability to attenuate overshoot and measurement noise compared to PI controller, and the relevant experimental results are demonstrated in [31].

B. Experimental Validation

In order to verify the effectiveness of the studied scheme, the comparative experiments based on the anti-windup PI controller, the conventional ADRC and the proposed VSADRC are performed on the PMSM test prototype, as presented in Fig. 10. Meanwhile, the key specifications of the experimental PMSM are summarized in Table I. In order to achieve a fair comparison of the three different strategies, the parameters of both conventional ADRC and the proposed VSADRC are set as $K_P = 30$ and $\omega_o = 300$ rad/s, i.e., $\beta_1 = 600$ and

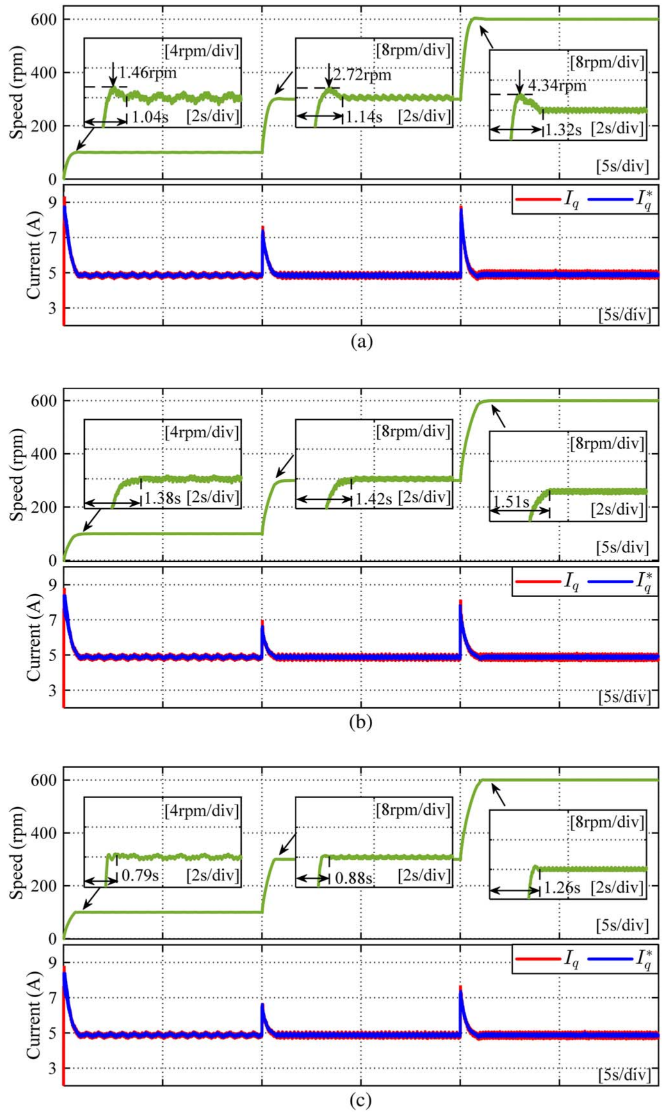

(a)

(b)

(c)

Fig. 11. Experimental results of speed step response and corresponding current curves with three different algorithms under rated load. (a) Anti-windup PI controller. (b) Conventional ADRC. (c) Proposed VSADRC.

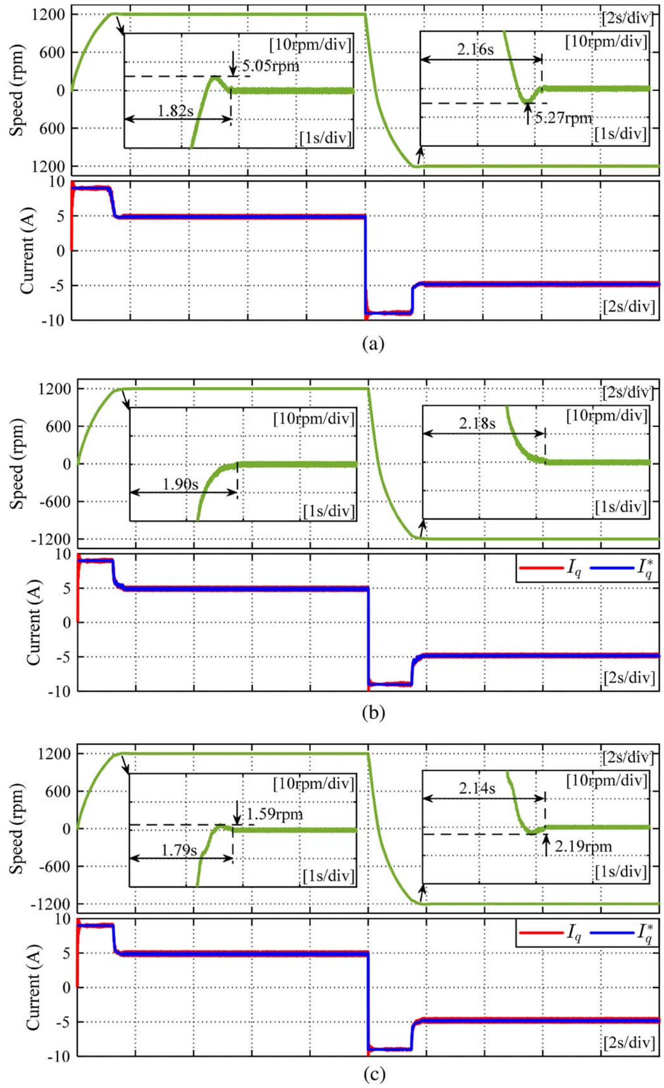

(a)

(b)

(c)

Fig. 12. Speed reversal and corresponding current experimental results at rated speed under rated load for three different algorithms. (a) Anti-windup PI controller. (b) Conventional ADRC. (c) Proposed VSADRC.

$\beta_2 = 90000$. According to Table I, $b_0 = (1/0.0425)$, so the parameters of the antiwindup PI speed controller are set as $k_{ps} = (90000 + 600 \times 30)/(600 + 30) \times 0.0425 \approx 7.286$ and $k_{is} = (90000 \times 30)/(600 + 30) \times 0.0425 \approx 182.143$ from Section V-A, and the antiwindup loop is introduced to in the integral term to attenuate the overshoot of the PI controller. Besides, the speed loop saturation is set to 9A to prevent excessive current. The control strategy is executed on a DSP-TMS320F28335, and a magnetic powder brake is employed to impose the external load. The speed loop sampling time is 0.001s, and the current loop sampling frequency is 8 KHz.

1) Dynamic Performance Experiment: In order to demonstrate the superior speed dynamics and disturbance rejection performance of the proposed algorithm, a series of experiments such as speed step, speed reversal, and load step are carried out from Figs. 11 to 14. First, Fig. 11 presents the step response and corresponding current curves of three different algorithms under rated load condition with speed steps from 0 to 100, 300, and 600 rpm. From Fig. 11, it can be observed that the anti-windup PI controller exhibits significant speed overshoot during speed steps, which are 1.46, 2.72, and 4.34 rpm respectively, while the conventional ADRC and the proposed VSADRC show almost no noticeable overshoot. It should be noted that the anti-windup PI can reduce the impact of overshoot to a certain extent, but it cannot completely eliminate overshoot. Besides, the settling time of the proposed VSADRC is 0.79, 0.88, and 1.26 s, which is shorter than that of the anti-windup PI controller (1.04, 1.14, and 1.32 s) and the conventional ADRC (1.38, 1.42, and 1.51 s). Consequently, the proposed VSADRC demonstrates the superior dynamic performance compared to the other two methods in step response tests.

Second, Figs. 12 and 13 show the speed reversal and corresponding current experiments of three different algorithms

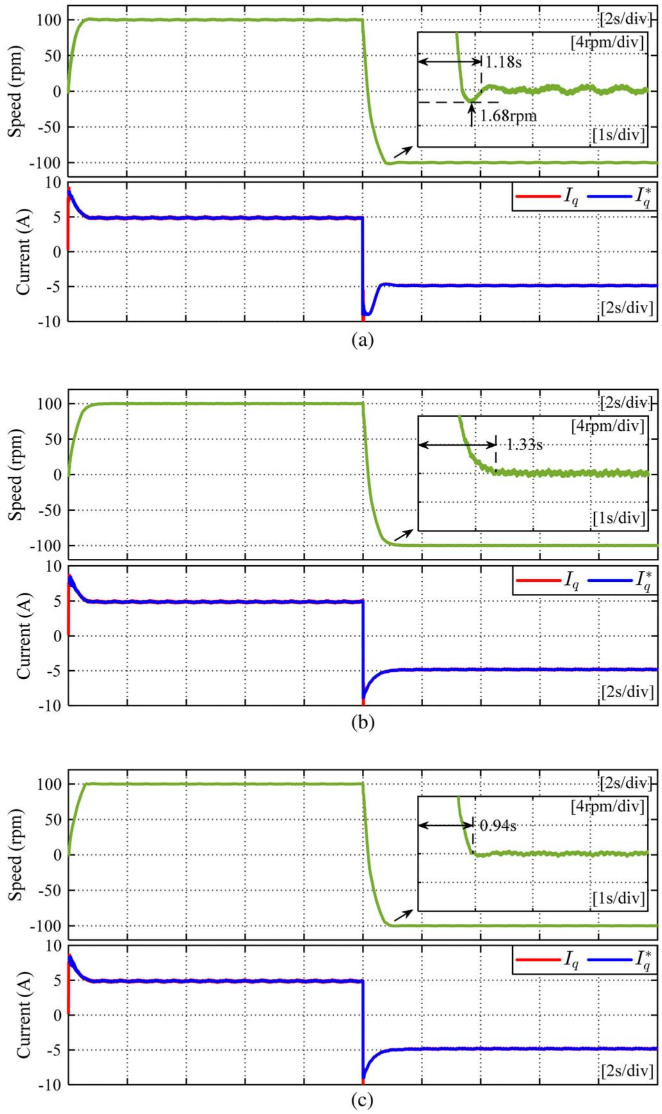

Fig. 13. Speed reversal and corresponding current experimental results at 100 rpm under rated load for three different algorithms. (a) Anti-windup PI controller. (b) Conventional ADRC. (c) Proposed VSADRC.

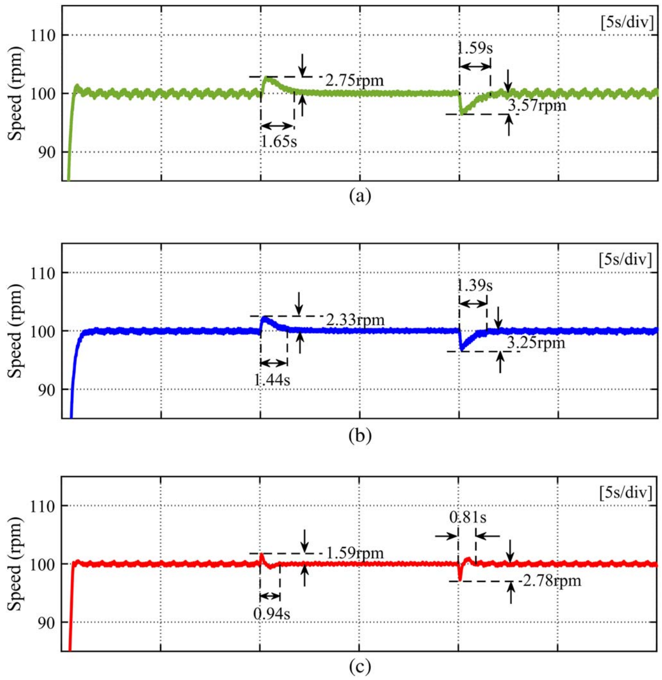

Fig. 14. Experimental results of sudden unloading and sudden loading of the rated load with three different algorithms. (a) Anti-windup PI controller. (b) Conventional ADRC. (c) Proposed VSADRC.

at rated speed and 100 rpm under rated load, respectively. From 12, it can be seen that when the speed steps to the rated speed, the overshoot of the antiwindup PI controller is 5.05 rpm, the ADRC shows no overshoot, and the proposed VSADRC introduces a slight overshoot of 1.59 rpm due to its preestimation of disturbances at high speeds. It should be noted that the proposed VSADRC still has the shortest settling time of 1.79 s. When the speed reverses from the positive rated speed to the negative rated speed, the overshoot for the antiwindup PI controller is 5.27 rpm, while for the VSADRC, it is 2.19 rpm. In terms of settling time, the VSADRC still has the shortest time of 2.14 s. Similarly, Fig. 13 shows the 100 rpm reversal experiment under rated load, and it can be found that both the proposed VSADRC and the conventional ADRC exhibit almost no overshoot, while the antiwindup PI controller has an overshoot of 1.68 rpm. The proposed VSADRC has the shortest settling time of 0.94 s, followed by the antiwindup PI controller with a settling time of 1.18 s, and the ADRC with the longest settling time of 1.33 s. Thus, it can be concluded that the proposed VSADRC demonstrates excellent dynamic performance in speed reversal.

Third, to verify the disturbance rejection performance of the proposed method, Fig. 14 presents the speed curves of sudden unloading and loading of the rated load for the three different algorithms. From Fig. 14, when the rated load is suddenly removed at 10 s, the speed rise of the antiwindup PI controller, ADRC and the proposed VSADRC is 2.75, 2.33, and 1.59 rpm, respectively, and the corresponding recovery time is 1.65, 1.44, and 0.94 s, respectively. Furthermore, when the rated load is suddenly applied at 20 s, the speed drop of the anti-windup PI controller, ADRC and the proposed VSADRC is 3.57, 3.25, and 2.78 rpm, respectively, and the corresponding recovery time is 1.59, 1.39, and 0.81 s, respectively. Accordingly, it can be concluded from Fig. 14 the presented algorithm has stronger disturbance rejection capability and shorter recovery time. In summary, the above experimental results demonstrate that the proposed VSADRC scheme exhibits superior speed dynamics and disturbance rejection performance.

2) Steady State Performance Experiment: In order to illustrate the excellent smooth speed regulation performance of the proposed scheme, Fig. 15 presents the comparative experimental results of the steady-state speed, the zoomed-in phase current, the phase current, and the corresponding fast Fourier transform (FFT) analysis of the steady-state speed of the three different methods under rated load. Due to the high signal-to-noise ratio at high speed, which masks a lot of frequency domain information, the speed employed in the following experiment is set to 100 rpm. From Fig. 15, the steady-state

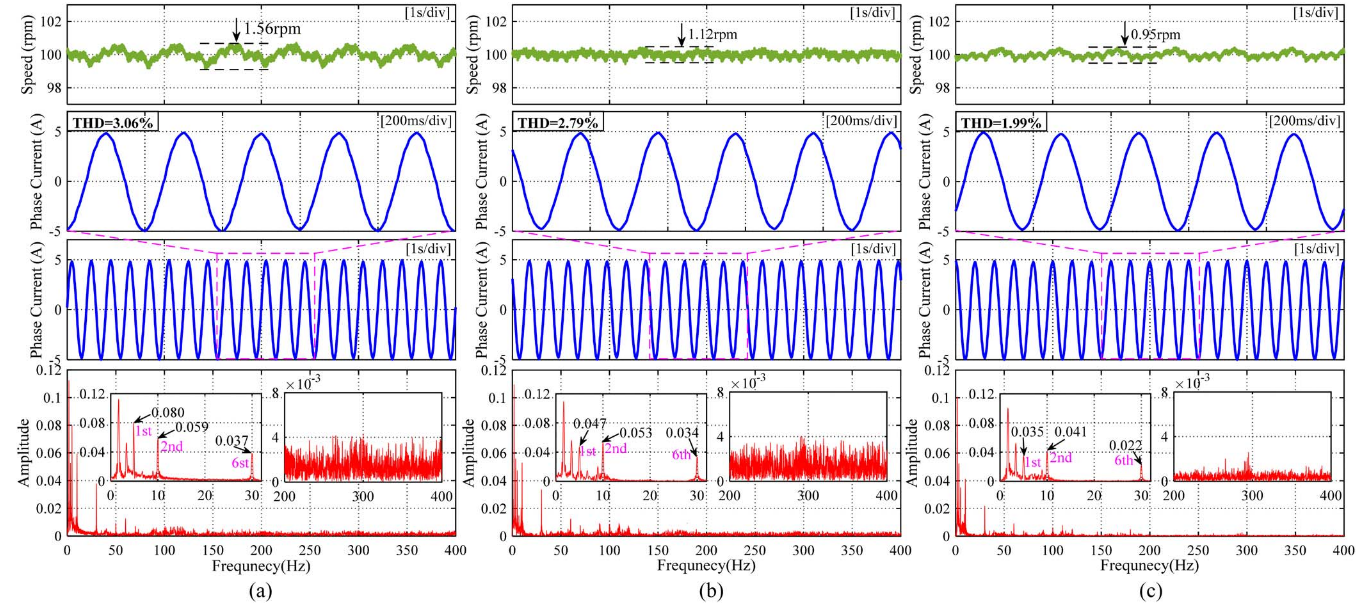

(a) (b) (c)

Fig. 15. Experimental results of the steady-state speed and phase current and FFT results of speed for three different methods under rated load. (a) Anti-windup PI controller. (b) Conventional ADRC. (c) Proposed VSADRC.

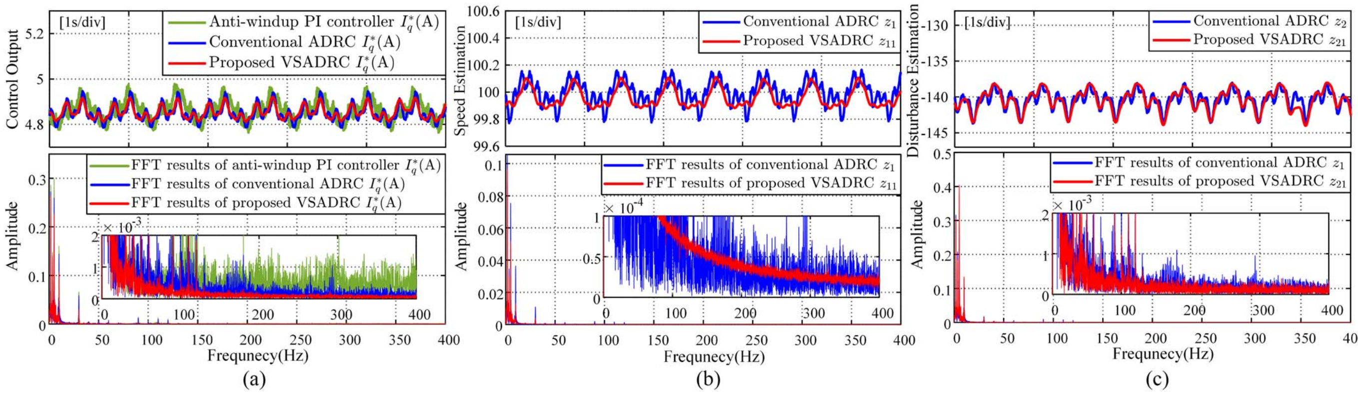

(a) (b) (c)

Fig. 16. Experimental results of q-axis current reference, speed estimation and disturbance estimation in the steady state and the corresponding FFT results under rated load. (a) Control output. (b) Speed estimation. (c) Disturbance estimation.

speed fluctuations of the antiwindup PI controller, the conventional ADRC and the proposed VSADRC are 1.56, 1.12, and 0.95 rpm, respectively, and their corresponding phase current total harmonic distortions (THD) are 3.06%, 2.79% and 1.99% respectively. Compared with the anti-windup PI controller and ADRC, the presented method reduces the steady-state speed fluctuation by 39.10% and 15.18%, respectively, and the THD of the phase current is decreased by 1.07% and 0.8% respectively. In addition, the FFT analysis results present that the amplitudes of the first and second harmonics caused by offset error and scaling error and the sixth harmonic caused by dead time of the proposed scheme are reduced compared with the antiwindup PI and ADRC, and the amplitude of VSADRC in the high frequency domain is also the smallest. Thus, it can be concluded that the proposed scheme can achieve smoother speed regulation performance than the conventional methods.

3) Noise Suppression Performance Experiment: In order to evaluate the noise suppression performance of the proposed method, Fig. 16 presents the controller output $I_q^*(A)$, observer output z_1, z_{11}, z_2, andz_{21}, and the corresponding FFT results of the proposed method and the conventional methods in the steady state under rated load. The noise situations can be evaluated by analyzing the noise amplitude in the control output and observer output according to the FFT results. It is obvious that the control output, speed estimation and disturbance estimation waveforms of the proposed VSADRC are more refined than the anti-windup PI controller and ADRC, which means that the high-frequency noise components of the proposed scheme are significantly attenuated. It should be pointed out that the most obvious fluctuation in the waveform is caused by low-frequency harmonic components rather than noise and its mechanical fluctuation frequency is $5/3$ Hz. According to the FFT analysis

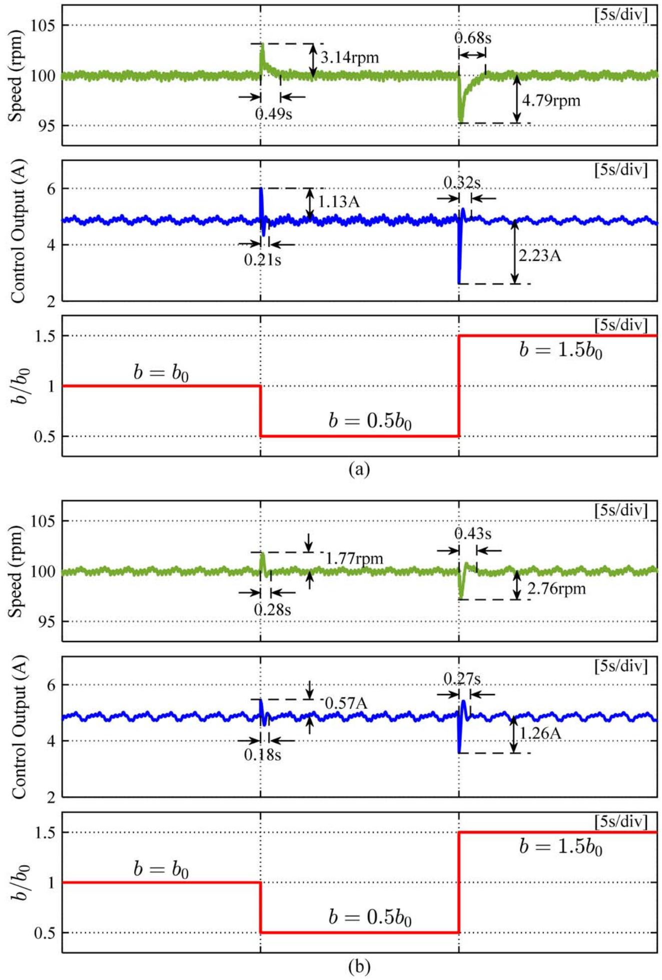

Fig. 17. Experimental results of speed and q-axis current reference of two different methods with parameter mismatch under rated load. (a) Conventional ADRC. (b) Proposed VSADRC.

results, it can be seen that the proposed VSADRC scheme is effective in reducing the amplitude of noise. Thus, it can be obtained that compared with the anti-windup PI controller and ADRC, the proposed VSADRC can achieve satisfactory noise suppression performance and more refined control and estimation output.

4) Parameter Robustness Experiment: In order to verify the parameter robustness of the proposed scheme, Fig. 17 shows the comparative experimental results of the conventional ADRC and the proposed VSADRC with the model control parameter b_0 variation under rated load. For each subfigure, from top to bottom are the speed, q-axis current reference and b_0 variation curves. From Fig. 17, under a sudden change in the control gain from b_0 to $0.5b_0$, the conventional ADRC experiences a speed change of 3.14 rpm and a recovery time of 0.49 s, whereas the proposed VSADRC shows a speed change of 1.77 rpm and a significantly shorter recovery time of 0.28 s. The control output changes for ADRC and VSADRC are 1.13 and 0.57 A, respectively, with the corresponding recovery times of 0.21 and 0.18 s. Similarly, when the control gain abruptly changes from $0.5b_0$ to $1.5b_0$, the speed variations for ADRC and VSADRC are 4.79 and 2.76 rpm, respectively, with the corresponding recovery time of 0.68 and 0.43 s. The control output variations for ADRC and VSADRC are 2.23 and 1.26 A, respectively, with the corresponding recovery time of 0.32 and 0.27 s. The robustness comparison under parameter mismatch is summarized in Table II. Thus, it can be concluded that the proposed VSADRC can achieve stronger robustness to parameter mismatch compared with the conventional ADRC, which is consistent with the analysis in Section IV-E.

TABLE II
ROBUSTNESS COMPARISON UNDER PARAMETER MISMATCH

	Parameter index	ADRC	VSADRC
$b_0 \rightarrow 0.5b_0$	Speed fluctuation	3.14 rpm	1.77 rpm
	Speed recovery time	0.49 s	0.28 s
	Control output fluctuation	1.13 A	0.57 A
	Control output recovery time	0.21 s	0.18 s
$0.5b_0 \rightarrow 1.5b_0$	Speed fluctuation	4.79 rpm	2.76 rpm
	Speed recovery time	0.68 s	0.43 s
	Control output fluctuation	2.23 A	1.26 A
	Control output recovery time	0.32 s	0.27 s

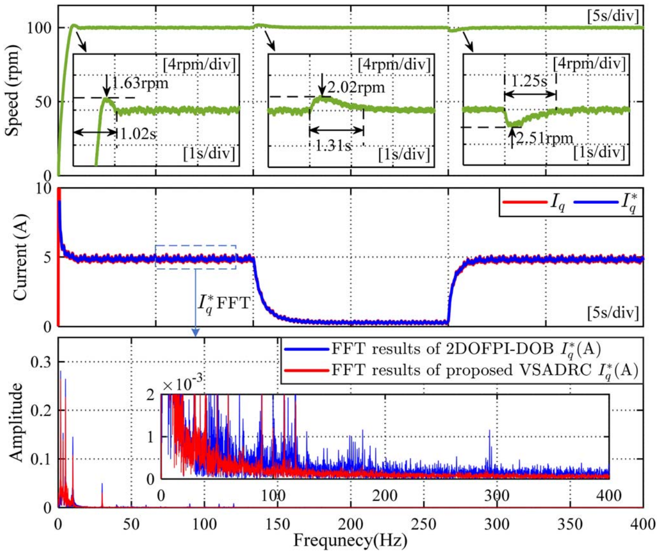

Fig. 18. Experimental results of speed step under rated load and sudden loading and unloading of rated load using the 2DOFPI-DOB [32] and comparison results of FFT analysis of control output.

5) Comparison With Two-Degree-of-Freedom PI and Disturbance Observer (2DOFPI-DOB) [32]: To further demonstrate the superior performance of the proposed method under the two-degree-of-freedom framework, it is further compared fairly with the 2DOFPI-DOB in reference [32] and the parameters of 2DOFPI-DOB are designed according to the tuning method of [32] with the same bandwidth as VSADRC. Fig. 18 presents the

TABLE III
PERFORMANCE COMPARISON OF 2DOFPI-DOB AND VSADRC

Parameter Index		2DOFPI-DOB [32]	VSADRC
Speed step	Speed overshoot	1.63 rpm	–
	Setting time	1.63 s	0.79 s
Remove rated load	Speed rise	2.02 rpm	1.59 rpm
	Recovery time	1.31 s	0.94 s
Add rated load	Speed drop	2.51 rpm	2.78 rpm
	Recovery time	1.25 s	0.81 s

TABLE IV
COMPUTATION BURDEN COMPARISON

Methods	Clock Cycles	Average Computation Time
Anti-windup PI controller	759	5.060 μs
Conventional ADRC	869	5.793 μs
2DOFPI-DOB [32]	1027	6.847 μs
Proposed VSADRC	1138	7.587 μs

experimental results of speed step under rated load and sudden loading and unloading of rated load using the 2DOFPI-DOB, and also shows the FFT comparison results of the q-axis current reference of 2DOFPI-DOB and VSADRC. It can be seen that 2DOFPI-DOB has overshoot during speed step, which is also verified in the experimental results of [32]. The overshoot of speed step is 1.63 rpm and the setting time is 1.02 s. From Fig. 18, when the rated load is suddenly removed, the speed rise of the 2DOFPI-DOB is 2.02 rpm, and the corresponding recovery time is 1.31 s. When the rated load is suddenly applied, the speed drop of the 2DOFPI-DOB is 2.51 rpm, and the corresponding recovery time is 1.25 s. The relevant performance comparison of the proposed VSADRC and 2DOFPI-DOB is summarized in Table III, and it can be found that the proposed VSADRC is superior to the 2DOFPI-DOB except that the speed drop under rated load is slightly greater than that of the 2DOFPI-DOB. In terms of noise suppression, the amplitude of the FFT analysis of the control output of the proposed VSADRC is smaller than that of the 2DOFPI-DOB, which indicates that the noise suppression performance of the proposed VSADRC is better than that of the 2DOFPI-DOB.

6) Computational Burden Comparison: In order to evaluate the performance of presented VSADRC in real-time calculation, the comparison of the execution time burden of the three methods on DSP is listed in Table IV. It is noted that the clock frequency of the employed 32-bit floating-point DSP-TMS320F28335 is 150 MHz. Thus, according to the clock cycles performed by the three different strategies, the corresponding execution time can be calculated. It can be known from Table IV that the average execution time of anti-windup PI, conventional ADRC, 2DOFPI-DOB and the proposed VSADRC is 5.060, 5.793, 6.847, and 7.587 μs, respectively. The method with the shortest execution time is PI, followed by the conventional ADRC, and the longest is the proposed VSADRC. Fortunately, the execution time of the presented scheme is much shorter than the control period of the speed loop, which is tolerable for the disturbance rejection enhancement and measurement noise improvement of PMSM speed control.

VI. CONCLUSION

In this article, a VSADRC scheme is developed for PMSM speed control, so as to enhance the disturbance rejection performance and improve the measurement noise suppression characteristic simultaneously. Specifically, the proposed VSESO adopts a two-stage interconnected observer structure, in which the extended disturbance differential is appended to the second-stage framework of VSESO to achieve higher-level disturbance estimation. Furthermore, the second-stage disturbance estimation in VSESO is employed for compensation to avoid using the signal directly contaminated by measurement noise. The slope of the magnitude curve is 40 dB/dec for the VSESO and 20 dB/dec for the ESO at low frequencies, and the slope of the magnitude curve is −40 dB/dec for the VSESO and −20 dB/dec for the ESO at high frequencies. The experimental investigations demonstrate that the proposed VSADRC has shorter settling time and less speed drop than the conventional methods, while the noise of output dynamic is significantly suppressed. Our future work will focus on dealing with the oscillation caused by the mid-frequency peak of the ADRC of the ramp-type disturbance rejection.

REFERENCES

[1] S. K. Kommuri, M. Defoort, H. R. Karimi, and K. C. Veluvolu, "A robust observer-based fault-tolerant control for PMSM in electric vehicles," *IEEE Trans. Ind. Electron.*, vol. 63, no. 12, pp. 7671–7681, Dec. 2016.

[2] H. Cao et al., "Generalized active disturbance rejection with reduced-order vector resonant control for PMSM disturbances suppression," *IEEE Trans. Power Electron.*, vol. 38, no. 5, pp. 6407–6421, May 2023.

[3] Y. Zuo, X. Ge, Y. Zheng, Y. Chen, H. Wang, and A. T. Woldegiorgis, "An adaptive active disturbance rejection control strategy for speed-sensorless induction motor drives," *IEEE Trans. Transport. Electrific.*, vol. 8, no. 3, pp. 3336–3348, Sep. 2022.

[4] B. Wang, M. Tian, Y. Yu, Q. Dong, and D. Xu, "Enhanced ADRC with quasi-resonant control for PMSM speed regulation considering aperiodic and periodic disturbances," *IEEE Trans. Transport. Electrific.*, vol. 8, no. 3, pp. 3568–3577, Sep. 2022.

[5] Z Sun et al., "Improved cascaded model-free predictive speed control for PMSM speed ripple minimization based on ultra-local model," *ISA Trans.*, vol. 143, pp. 666–677, Dec. 2023.

[6] J. Yang, W. H. Chen, S. Li, L. Guo, and Y. Yan, "Disturbance/uncertainty estimation and attenuation techniques in PMSM drives—A survey," *IEEE Trans. Ind. Electron.*, vol. 64, no. 4, pp. 3273–3285, Apr. 2017.

[7] T. Yang, Y. Deng and H. Li, "Fast integral terminal sliding mode control with a novel disturbance observer based on iterative learning for speed control of PMSM," *ISA Trans.*, vol. 134, pp. 460–471, Mar. 2023.

[8] J. Han, "From PID to active disturbance rejection control," *IEEE Trans. Ind. Electron.*, vol. 56, no. 3, pp. 900–906, Mar. 2009.

[9] Z. Gao, "Scaling and bandwidth-parameterization based controller tuning," in *Proc. Amer. Control Conf.*, 2003, pp. 4989–4996.

[10] E. Sariyildiz, R. Oboe, and K. Ohnishi, "Disturbance observer-based robust control and its applications: 35th anniversary overview," *IEEE Trans. Ind. Electron.*, vol. 67, no. 3, pp. 2042–2053, Mar. 2020.

[11] S. Ahmad and A. Ali, "On active disturbance rejection control in presence of measurement noise," *IEEE Trans. Ind. Electron.*, vol. 69, no. 11, pp. 11600–11610, Nov. 2022.

[12] C. Liu, G. Luo, X. Duan, Z. Chen, Z. Zhang, and C. Qiu, "Adaptive LADRC-based disturbance rejection method for electromechanical servo system," *IEEE Trans. Ind. Appl.*, vol. 56, no. 1, pp. 876–889, Jan. 2020.

[13] Q. Hou et al., "Enhanced active disturbance rejection control with measurement noise suppression for PMSM drives via augmented nonlinear extended state observer," *IEEE Trans. Energy Convers.*, vol. 39, no. 1, pp. 287–299, Mar. 2024.

[14] Z. Yin, C. Du, J. Liu, X. Sun, and Y. Zhong, "Research on disturbance-rejection control of induction motors based on an ant colony optimization algorithm," vol. 65, no. 4, pp. 3077–3094, Apr. 2018.

[15] Y. Wang, S. Fang, and J. Hu, "Active disturbance rejection control based on deep reinforcement learning of PMSM for more electric aircraft," *IEEE Trans. Power Electron.*, vol. 38, no. 1, pp. 406–416, Jan. 2023.

[16] A. A. Prasov and H. K. Khalil, "A nonlinear high-gain observer for systems with measurement noise in a feedback control framework," *IEEE Trans. Autom. Control*, vol. 58, no. 3, pp. 569–580, Mar. 2013.

[17] Y. Zuo, J. Mei, C. Jiang, X. Yuan, S. Xie, and C. H. T. Lee, "Linear active disturbance rejection controllers for PMSM speed regulation system considering the speed filter," *IEEE Trans. Power Electron.*, vol. 36, no. 12, pp. 14579–14592, Dec. 2021.

[18] Y. Du, W. Cao, and J. She, "Analysis and design of active disturbance rejection control with an improved extended state observer for systems with measurement noise," *IEEE Trans. Ind. Electron.*, vol. 70, no. 1, pp. 855–865, Jan. 2023.

[19] H. Sun, R. Madonski, S. Li, Y. Zhang, and W. Xue, "Composite control design for systems with uncertainties and noise using combined extended state observer and Kalman filter," *IEEE Trans. Ind. Electron.*, vol. 69, no. 4, pp. 4119–4128, Apr. 2022.

[20] K. Łakomy and R. Madonski, "Cascade extended state observer for active disturbance rejection control applications under measurement noise," *ISA Trans.*, vol. 109, pp. 1–10, Mar. 2021.

[21] K. Łakomy et al., "Active disturbance rejection control design with suppression of sensor noise effects in application to DC-DC buck power converter," *IEEE Trans. Ind. Electron.*, vol. 69, pp. 816–824, Jan. 2022.

[22] H. Cao et al., "Improved ADRC with a cascade extended state observer based on quasi-generalized integrator for PMSM current disturbances attenuation," *IEEE Trans. Transp. Electr.*, vol. 10, no. 1, pp. 2145–2157, Mar. 2024.

[23] O. Babayomi and Z. Zhang, "Model-free predictive control of power converters with multifrequency extended state observers," *IEEE Trans. Ind. Electron.*, vol. 70, no. 11, pp. 11379–11389, Nov. 2023.

[24] L. Tao, P. Wang, X. Ma, Y. Wang, and X. Zhou, "Variable form LADRC-based robustness improvement for electrical load interface in microgrid: a disturbance response perspective," *IEEE Trans. Ind. Informat.*, vol. 20, no. 1, pp. 432–441, Jan. 2024.

[25] Z. Yan, S. Deng, Z. Yang, Y. Wang, Y. Lu, and X. Shi, "An ADRC strategy with sequential output stacking extended state observers to evaluate hydraulic torque for a continuous-wave pulse generator," *IEEE Trans. Ind. Informat.*, vol. 20, no. 3, pp. 4259–4270, Mar. 2024.

[26] Y. Zuo, J. Chen, X. Zhu, and C. H. T. Lee, "Different active disturbance rejection controllers based on the same order GPI observer," *IEEE Trans. Ind. Electron.*, vol. 69, no. 11, pp. 10969–10983, Nov. 2022.

[27] H. Cao et al., "Unified interpretation of active disturbance rejection control for electrical drives," *IEEE Trans. Circuits Syst. II, Exp. Briefs*, vol. 71, no. 7, pp. 3433–3437, Jul. 2024.

[28] H. Jin et al., "On the characteristics of ADRC: A PID interpretation," *Sci. China Inf. Sci.*, vol. 63, pp. 258–260, Oct. 2020.

[29] M. Safonov, A. Laub, and G. Hartmann, "Feedback properties of multivariable systems: The role and use of the return difference matrix," *IEEE Trans. Autom. Control*, vol. 26, no. 1, pp. 47–65, Feb. 1981.

[30] H. Jin et al., "Replacing PI control with first-order linear ADRC," in *Proc. IEEE 8th Data Driven Control Learn. Syst. Conf.*, 2019, pp. 1097–1101.

[31] B. Guo et al., "A phase-locked loop using ESO-based loop filter for grid-connected converter: performance analysis", *Control Theory Technol.*, vol. 19, pp. 49–63, Mar. 2021.

[32] Y. Fan, J. Chen, Q. Zhang and M. Cheng, "An improved inertia disturbance suppression method for PMSM based on disturbance observer and two-degree-of-freedom PI controller," *IEEE Trans. Power Electron.*, vol. 38, no. 3, pp. 3590–3599, Mar. 2023.

Haiyang Cao (Graduate Student Member, IEEE) was born in Shandong, China, in 1997. He is currently working toward the Ph.D. degree in mechatronic engineering with the University of Chinese Academy of Sciences, Beijing, China, and Changchun Institute of Optics, Fine Mechanics and Physics, Chinese Academy of Sciences, Changchun, China.

Since 2023, he has started as a Visiting Ph.D. Student with Nanyang Technological University, Singapore. His research interests include advanced control theories and applications on motor drive systems.

Yongting Deng (Senior Member, IEEE) was born in Shandong, China, in 1987. He received the B.E. degree in automation from China University of Petroleum (East China), Qingdao, China, in 2010, and the M.S. and Ph.D. degrees in mechatronic engineering from Changchun Institute of Optics, Fine Mechanics and Physics, Chinese Academy of Sciences, Changchun, China, in 2015.

He is currently a Professor with Changchun Institute of Optics, Fine Mechanics and Physics, Chinese Academy of Sciences. He has authored or coauthored more than 70 publications in the research interests that include controller design for ac motor drives and linear motor drives, intelligent control, and high-precision machine control techniques.

Yuefei Zuo (Member, IEEE) received the B.Eng. degree in electrical engineering and automation and the Ph.D. degree in power electronics and electrical drives from Nanjing University of Aeronautics and Astronautics, Nanjing, China, in 2010 and 2016, respectively.

He is currently a Full Professor with the College of Automation Engineering, Nanjing University of Aeronautics and Astronautics. In 2023, he joined the Department of Aeronautical and Automotive Engineering, Loughborough University, Loughborough, U.K., as a Research Associate. In 2019, he joined the School of Electrical and Electronic Engineering, Nanyang Technological University, Singapore, as a Research Fellow, and was promoted to a Senior Research Fellow in 2022. From 2016 to 2019, he was a Lecturer with the School of Electrical and Information Engineering, Jiangsu University, Zhenjiang, China. His research interests include power electronics, electric machines and drives, active disturbance rejection control, model predictive control, and artificial intelligence (AI).

Xiufeng Liu was born in Changchun, China, in 1998. He received the B.E. degree in vehicle engineering from Changchun University of Technology, Changchun, in 2020. He is currently working toward the Ph.D. degree in mechatronic engineering with the University of Chinese Academy of Sciences, Beijing, China, and Changchun Institute of Optics, Fine Mechanics and Physics, Chinese Academy of Sciences, Changchun.

His research interests include ac motor drive, sliding mode control, neural network, and digital control using a digital signal processor.

Jianli Wang (Member, IEEE) was born in Shandong, China, in 1971. He received the Ph.D. degree in mechatronic engineering from Changchun Institute of Optics, Fine Mechanics and Physics, Chinese Academy of Sciences, Changchun, China, in 2002.

He is currently a Professor with Changchun Institute of Optics, Fine Mechanics and Physics, Chinese Academy of Sciences. He has authored or coauthored more than 100 publications in his main areas of research, which are optical-electric telescope, high-resolution imaging, and high-precision machine control techniques.

Christopher H. T. Lee (Senior Member, IEEE) received the B.Eng. (First Class Hons.) and the Ph.D. degrees from the Department of Electrical and Electronic Engineering, The University of Hong Kong, Hong Kong, in 2009 and 2016, respectively, both in electrical engineering.

He is currently an Associate Professor with Nanyang Technological University, Singapore. He was a Postdoctoral Fellow and then a Visiting Assistant Professor with Massachusetts Institute of Technology, Cambridge, MA, USA. He is an Associate Editor for IEEE TRANSACTIONS ON INDUSTRIAL ELECTRONICS, IEEE TRANSACTIONS ON ENERGY CONVERSION, IEEE ACCESS, and *IET Renewable Power Generation*. He is the Chair of IEEE Vehicular Technology Society Singapore Section Chapter in 2023–2025. He is a Chartered Engineer in Hong Kong. His research interests include electric machines and drives, renewable energies, and electromechanical propulsion technologies. In these areas, he has published two books, four books chapters, and over 270 referred papers.

Dr. Lee was a recipient of the 10th Nagamori Award in 2024, IAS Myron Zucker Student-Faculty Grant in 2023, JSPS Fellowship in 2023, MDPI Energies Young Investigator Award in 2022, NRF Fellowship in 2020, Nanyang Assistant Professorship in 2019, Li Ka Shing Prize (the Best Ph.D. Thesis Prize) in 2017 and Croucher Foundation Fellowship in 2016, and five best paper awards, including First Place Best Paper Award in IEEE Transactions on Energy Conversion in 2022.